ORIGINAL PAPER

Composite Nanoarchitectonics of LaNi$_{0.95}$Fe$_{0.05}$O$_3$/Muscovite for Enhanced Photocatalytic Activity

Li Zeng · Tongjiang Peng · Hongjuan Sun · Xiyue Zhang · Jingjie Yang

Abstract Powder-type semiconductor photocatalysts are widely applicable but their defects (e.g. easy agglomeration during preparation and recyclability in the suspension system) limit their practical application. In the current study, perovskite oxide photocatalytic material was loaded onto a muscovite substrate to overcome the problems of low stability, easy agglomeration, and difficult recovery. A photocatalytically active LaNi$_{0.95}$Fe$_{0.05}$O$_3$/muscovite composite material was synthesized by a sol-gel impregnation method. Phase composition, morphology, and interfacial interaction of the composites, denoted as LNFBY-x (x: mass ratio of LNF to muscovite), were characterized by X-ray diffraction (XRD), scanning electron microscopy (SEM), transmission electron microscopy (TEM), X-ray photoelectron spectroscopy (XPS), and other analytical methods. According to the results, the particle size of LNF nanoparticles was regulated effectively by compounding with muscovite, and the agglomeration of LNF decreased. LNF nanoparticles were distributed evenly and attached in dense fashion to the surface of muscovite, thereby increasing the contact area with the reaction medium. The nanoparticles were connected to the silicon-oxygen tetrahedral sheet of the muscovite via Si–O–La, Si–O–Ni, and Si–O–Fe bonds, which increased the bonding strength between the composite components and expedited the transfer of photogenerated charge. More highly active oxygen species were produced, and a growing number of chemically active moieties (O_2^- and OH) was generated in the photocatalytic reaction. LNFBY-1.00 demonstrated the best photocatalytic activity. A degradation rate of methyl orange of 99.03% was achieved after visible-light irradiation for 120 min, which decreased to 75.75% after five repeated uses, thereby indicating high stability and recycling ability. The photocatalytic LaNi$_{0.95}$Fe$_{0.05}$O$_3$/muscovite composite material exhibited potential for application in environmental remediation practices.

Keywords Composite · Doping · Muscovite · Perovskite · Photocatalysis

Associate Editor: Yael Mishael

L. Zeng · T. Peng · H. Sun (✉) · X. Zhang · J. Yang
Education Ministry Key Laboratory of Solid Waste Treatment and Resource Recycle, Southwest University of Science and Technology, Mianyang 621010, China
e-mail: sunhongjuan@swust.edu.cn

Introduction

Semiconductor photocatalysis technology has promising applications in environmental protection, solar energy utilization, and the development of novel functional materials (Fukina et al., 2021; Shi et al., 2017; Tun et al., 2019). It refers to a new technology with major economic and social benefits. Among numerous photocatalytic materials, perovskite oxides (ABO$_3$) are recognized as p-type photocatalytic semiconductor materials with stable structures, narrow band positions, and prominent photocatalytic activity (Gong et al., 2019; Ismael &

Wu, 2019; Li et al., 2017b). However, the disadvantages of pure perovskite oxide catalytic materials (e.g. uncontrollable particle size, easy agglomeration, and poor recyclability) limit their practical application to a significant extent (Maeda et al., 2014; Peng et al., 2016; Purohit et al., 2021).

Over the past few years, a wide range of techniques has been developed to adjust and improve the performance of perovskite oxide photocatalytic materials (e.g. ion doping (Kim et al., 2019), surface loading (Li et al., 2017a), morphology control (Maridevaru et al., 2020), and heterostructure construction (Khaledian et al., 2021)). Loading photocatalytic nanoparticles on the surfaces of matrix materials is effective in controlling the size of nanoparticles and increasing the specific surface area and the number of active sites, while also overcoming the inherent lack of stability, agglomeration, and the problematic reuse of unsupported nanoparticles (Belver et al., 2016; Chen et al., 2019b; Khan et al., 2020; Landge et al., 2021; Yang et al., 2010). It is necessary, therefore, to attach perovskite oxide particles to a suitable matrix.

Muscovite is a layered silicate mineral with many advantages, such as good light transmittance, large specific surface area, strong adsorption capacity, good heat resistance, and stable chemical properties (Barakat et al., 2021; Salam et al., 2020; Shao et al., 2021; Touaa et al., 2020); an ideal natural catalyst carrier. A nano-zerovalent iron (NZVI)-loaded muscovite composite was synthesized by Bao et al. (2020) using a liquid-phase reduction method. This process prevented agglomeration, improved dispersibility, increased the number of catalytically active sites, and enhanced catalytic performance. A TiO$_2$/muscovite nanocomposite was synthesized by Li et al. (2019) using a liquid-phase precipitation method and those authors found that the muscovite matrix delayed growth and phase transformation of TiO$_2$ and enhanced photocatalytic activity. When perovskite oxide is loaded on the surface of muscovite, the structure and interfacial properties of the material will be changed, which is expected to improve the photocatalytic activity of the material.

In view of this, the purpose of the current study was to prepare photocatalytic LaNi$_{0.95}$Fe$_{0.05}$O$_3$/muscovite composite materials by a sol-gel method to obtain materials with high photocatalytic degradation performance and recyclability, while reducing their amount and preparation costs, which are critical criteria for the industrial application of such photocatalysts.

Materials and Methods

Materials

The initial components used for the production of photocatalytic LaNi$_{0.95}$Fe$_{0.05}$O$_3$/muscovite composite material were as follows: lanthanum nitrate (La(NO$_3$)$_3$·6H$_2$O) (analytically pure, produced by Shanghai Aladdin Biochemical Technology Co., Ltd, Shanghai, China); nickel nitrate (Ni(NO$_3$)$_2$·6H$_2$O), and ferric nitrate (Fe(NO$_3$)$_3$·9H$_2$O) (analytically pure, produced by Chengdu Kelong Chemical Reagent Factory, Chengdu, China). Citric acid (analytically pure, produced by Chengdu Kelong Chemical Reagent Factory, Chengdu, China) served as a complexing agent, and muscovite (K{Al$_2$[AlSi$_3$O$_{10}$](OH)$_2$}) (600 mesh, obtained from Shijiazhuang Chenxing Industrial Co., Ltd, Shijiazhuang, China) was the supporting matrix. Other materials used were: methyl orange, sodium sulfite (Na$_2$SO$_3$), ammonium oxalate ((NH$_4$)$_2$C$_2$O$_4$), isopropanol (IPA), and anhydrous ethanol (analytically pure, produced by Chengdu Kelong Chemical Reagent Factory, Chengdu, China); deionized water (resistivity of 18.2 MΩ·cm, prepared in the laboratory).

Preparation of LaNi$_{0.95}$Fe$_{0.05}$O$_3$/muscovite Composite Photocatalytic Material

In a beaker, 4.3301 g of La(NO$_3$)$_3$·6H$_2$O, 2.7625 g of Ni(NO$_3$)$_2$·6H$_2$O, and 0.2020 g of Fe(NO$_3$)$_3$·9H$_2$O were dissolved in 60 mL of a mixture of anhydrous ethanol and deionized water with a volume ratio of 2:1. Citric acid was added to the beaker in a molar ratio of 1.5:1 to the total amount of metal ions, ammonia water was added dropwise to regulate the pH to 7, and muscovite, calcined at 600°C for 3 h, was added in various mass ratios. The solution was stirred for 10 min at ambient temperature and shaken in an ultrasonic water bath for 10 min. The sample beaker was placed in a thermostatic water bath and stirred at 70°C until a gel was formed. The gel was frozen in a freezer and then dried in a freeze-dryer for 48 h to obtain a dry gel sample. The prepared dry gel was placed in a muffle furnace and heated to 600°C at a rate of 5°C·min^{-1}. After

⚫ Springer

natural cooling, the sample was ground into a powder for later use. The materials prepared with various $LaNi_{0.95}Fe_{0.05}O_3$ to muscovite ratios (x) were named LNFBY-x, where LNF denotes $LaNi_{0.95}Fe_{0.05}O_3$, BY represents the calcined muscovite, and x is the mass ratio of LNF to muscovite. The amounts of muscovite added in the various samples are listed in Table 1 and the preparation process is illustrated in Fig. 1.

Characterization

The phase composition of the samples was studied using an Ultima IV X-ray diffractometer (XRD, Rigaku Co., Tokyo, Japan) with CuKα radiation (λ = 1.5406 nm) over an angular range of 10–65°2θ, and continuous scanning with X'Clelerator. The morphology of each composite was examined using an Ultra 55 field emission scanning electron microscope (SEM, Zeiss, Oberkochen, Germany) with a working voltage of 15 kV, for which the samples were spread onto aluminum sheets and coated with a thin layer of gold by sputter coating. Transmission electron microscopy (TEM) and high-resolution TEM (HRTEM) were performed using an FEI Tecnai G20 instrument (Thermo Fisher Scientific, Inc., Waltham, Massachusetts, USA) with a LaB6 electron gun filament, operated at 200 kV. Surface potentials were measured using a Zetasizer Nano ZS90 instrument (Malvern Panalytical Co., Ltd., Malvern, UK). Specific surface area and porosity were determined by N_2 adsorption and desorption using an Autosorb IQ instrument (Anton Paar QuantaTec Inc., Boynton Beach, Florida, USA). The elemental analysis was performed on a K-Alpha$^+$-type X-ray photoelectron spectrometer (XPS, Thermo Fisher Scientific, Inc., Waltham, Massachusetts, USA), using a monochromatic AlKα source with an energy of 1486.6 eV. The IR absorption characteristics of the composites were investigated as KBr disks using a Nicolet-5700 FTIR spectrometer (Nicolet Instrument Co., Ltd., Fitchburg, Massachusetts, USA). The absorbance of the supernatant in the catalytic tests was measured by an Evolution 300 UV-Vis spectrophotometer (Thermo Fisher Scientific, Inc., Waltham, Massachusetts, USA).

Photocatalytic Performance Test

To assess the photocatalytic performance of the LNFBY-x composite materials in visible light, methyl orange (MO) was selected as the target pollutant, and a xenon lamp (HEL-HXF300, Beijing Zhongjiao Jinyuan Technology Co., Ltd., Beijing, China) acted as the light source with a 400–800 nm filter. In a beaker, 100 mg of photocatalytic material was dispersed in 100 mL of a 10 mg·L^{-1} MO solution . The light source was attached to a magnetic stirrer at a distance of 20 cm from the liquid surface of the solution, which was then stirred for 1 h in the dark to ensure that adsorption-desorption equilibrium between photocatalyst and dye was reached. The light source was switched on, and 5 mL of solution was sampled every 20 min and centrifuged to remove the catalyst particles. The absorbance of the supernatant was examined at the maximum absorption wavelength of MO at 437 nm, and the degradation percentage D of MO was calculated by:

$$D = (C_0 - C_t)/C_0 \tag{1}$$

where C_0 denotes the initial MO concentration and C_t represents the MO concentration after a certain reaction time (mg·L^{-1}).

Active Free Radical Test

To illustrate the photocatalytic degradation mechanism of the samples, free-radical tests were performed by applying sodium sulfite (Na_2SO_3) as an electron (e$^-$) trapping agent, ammonium oxalate (($NH_4)_2C_2O_4$) as a hole (h$^+$) trapping agent, and isopropanol (IPA) as an hydroxyl radical (OH) trapping agent. 100 mg of catalyst and 0.17 mmol of the free-radical

Table 1 Muscovite added to $LaNi_{0.95}Fe_{0.05}O_3$/muscovite composite photocatalytic material

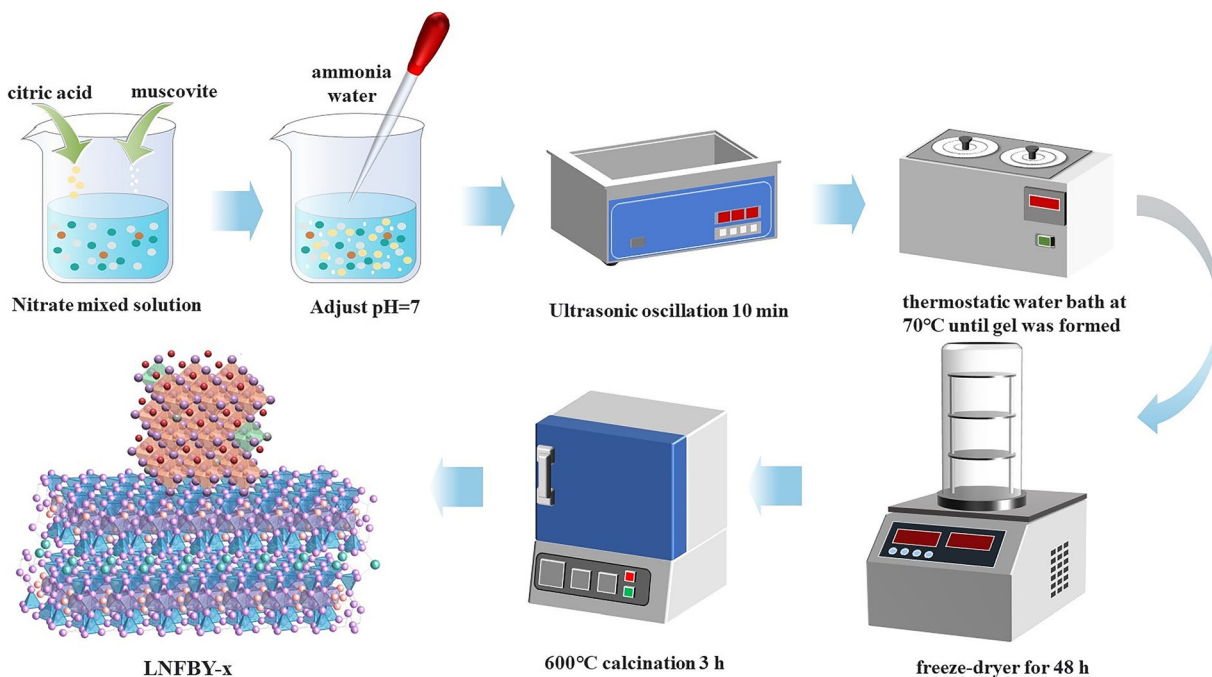| Sample number	Amount of muscovite added (g)
LNF	0.00
LNFBY-5.00	0.40
LNFBY-1.67	1.20
LNFBY-1.00	2.00
LNFBY-0.71	2.80
LNFBY-0.56	3.60
LNFBY-0.50	4.00

Fig. 1 Process of preparing the LNFBY-1 sample

scavenger were dispersed in 100 mL of 10 mg·L^{-1} MO solution, and the photocatalytic performance test was conducted to determine the main active substances during photodegradation.

Results and Discussion

Phase and Structural Characteristics

The XRD patterns of the LNFBY-x samples (Fig. 2) revealed that the muscovite sample (BY) has diffraction peaks characteristic of $2M_1$-type muscovite (JCPDS 46-1409) ($d_{002} = 0.9835$ nm, $d_{004} = 0.4989$ nm, $d_{006} = 0.3307$ nm, and $d_{115} = 0.3187$ nm) and of quartz (JCPDS 79-1906) ($d_{100} = 0.4252$ nm, $d_{011} = 0.3336$ nm, and $d_{021} = 0.1991$ nm) were present, indicating that the sample was $2M_1$-type muscovite with a small amount of quartz impurity. The diffraction peaks of the LNF sample ($d_{100} = 0.3855$ nm, $d_{110} = 0.2727$ nm, $d_{111} = 0.2213$ nm, $d_{200} = 0.1927$ nm, and $d_{210} = 0.1704$ nm) conformed to those of the standard spectrum of cubic perovskite phase (JCPDS 33-0710). The XRD peaks of all LNFBY-x composite samples were consistent with those of LNF and muscovite. The intensity of the

muscovite diffraction peaks increased with increasing muscovite amount, which demonstrated that the introduction of LNF retained the muscovite structure.

Morphology, Structure, and Composition Characteristics

The SEM and TEM images of the BY, LNF, and LNFBY-1.00 samples (Fig. 3) showed that muscovite used in the experiment displayed a layered structure with a diameter of nearly 20 μm and a flake diameter to thickness ratio of ~2:1 (Fig. 3a). In addition, its surface was smooth and flat, laying a solid foundation for loading LNF. The pure LNF sample consisted of spherical particles with a particle size of ~50 nm with poor dispersion and obvious agglomeration (Fig. 3b). The SEM images of LNFBY-1.00 (Figs 3c and 3d) revealed that LNF nanoparticles were loaded successfully onto the surface of muscovite, forming a dense film layer. The particle size in the LNFBY-1.00 sample was close to 20 nm, which is significantly smaller than that of pure LNF, and agglomeration was significantly inhibited.

These observations were related to the abundant active sites on the surface of muscovite, assisting in controlling the growth of LNF grains (Tahir et al., 2019).

Fig. 2 XRD patterns of LNFBY-
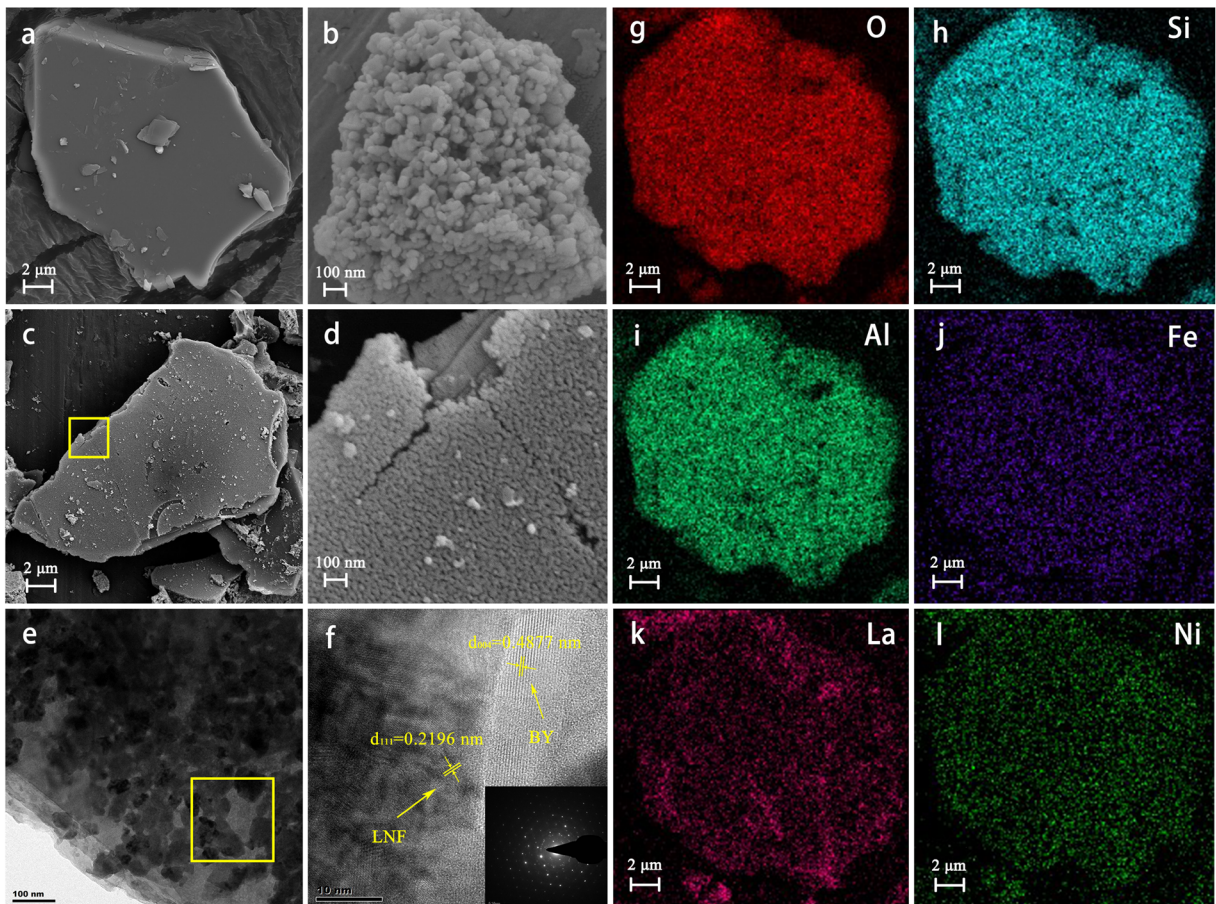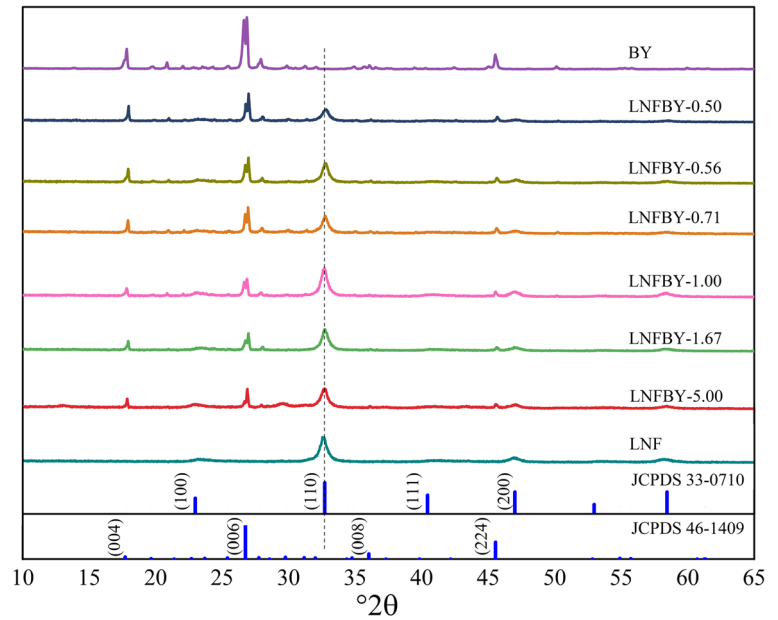*x* samples over the range
10–65°2θ

Fig. 3 **a** SEM image of BY; **b** SEM image of LNF; **c** SEM image of LNFBY-1.00; **d** SEM image of LNFBY-1.00; **e–f** HRTEM images of LNFBY-1.00; **g–l** EDS mapping images of LNFBY-1.00

🖄 Springer

The HRTEM images (Figs 3e and 3f) revealed that the LNFBY-1.00 sample featured easily identifiable lattice stripes, which demonstrated the crystallinity of the sample. The measured lattice spacings of $d = 0.4877$ nm and $d = 0.2196$ nm corresponded to the (004) crystal plane of muscovite and the (220) crystal plane of LNF, respectively. Through energy-dispersive X-ray spectroscopy (EDS), the element proportions of the sample were determined (Table 2); in addition to the elements present in muscovite (O, Si, Al, and K) and Au generated during sample preparation, the LNFBY-1.00 sample also contained the elements (La, Ni, and Fe) present in LNF. EDS mapping of LNFBY-1.00 (Figs 3g–l) further verified that LNF was loaded successfully on the surface of muscovite without destroying the structure or changing the chemical composition of muscovite during the synthesis process.

The surface zeta potential curves of muscovite and the LNF precursor over a range of pH values (Fig. 4) showed that the zeta potential of muscovite was negative at pH 7, the preparation stage, while that of the LNF precursor sol was positive. Consequently, when muscovite was suspended and dispersed in the LNF precursor sol, the two components, impacted by different surface charges, were attracted and bound to each other electrostatically. The positively charged LNF precursor sol nucleated and grew on the negatively charged muscovite surface, forming a coating layer that does not detach easily (Zhou et al., 2012). Due to the chemical bonding, the two components were combined firmly, thereby improving utilization and recyclability.

Nitrogen Adsorption-desorption Isotherms and NLDFT Pore-size Distribution

The nitrogen adsorption-desorption isotherms and Nonlocal-Density-Functional-Theory (NLDFT) pore-size distribution of the BY, LNF, and LNFBY-1.00 samples (Fig. 5a) showed that the adsorption-desorption isotherms of the muscovite sample had almost no hysteresis loop, while LNF and LNFBY-1.00 exhibited the typical type-II characteristics (Xu et al., 2019), which demonstrated their mesoporous structure. The specific surface areas of the BY, LNF, and LNFBY-1.00 samples were calculated as 3.237 $m^2 \cdot g^{-1}$, 11.055 $m^2 \cdot g^{-1}$, and 8.412 $m^2 \cdot g^{-1}$, respectively. The NLDFT method was used to study further the pore-size distribution of the three samples (Fig. 5b), which showed that muscovite exhibited

micropores and mesopores. The micropores may come from the surface of muscovite, and the mesopores may come from the laminar structure of muscovite. LNF had a wide pore-size distribution. The smaller pore size may originate from single LNF nanoparticles, while the larger pore size may be attributed to agglomeration of LNF nanoparticles. The average pore size of LNFBY-1.00 was concentrated at 14.7 nm, and the pore-size distribution was relatively reduced, probably because LNF nanoparticles were loaded on the surface of muscovite, which reduced agglomeration and occupied the original micropores on the surface of muscovite. Compared with LNF, LNFBY-1.00 demonstrated a moderate specific surface area and pore-size distribution, which could provide more adsorption sites and photocatalytic active sites, thereby improving photocatalytic activity.

Molecular Vibration and Bond-energy Changes

The FTIR absorption bands in the BY, LNF, and LNFBY-1.00 samples (Fig. 6a) at 3449.94 and 1637.62 cm^{-1} were attributed to the stretching and bending vibrations of adsorbed H_2O, respectively (Khatri & Rana, 2020). The absorption bands at 3619.61 and 1006.18 cm^{-1} belonged to the stretching vibration of hydroxyl groups (–OH) (Edward, 1982; Peng et al., 2018) and the Si–O bond (Asencios et al., 2019; Wang et al., 2019), respectively. The bending vibration of Si–O produce the bands at 503.67 and 409.78 cm^{-1} (Farmer, 1968; Shi et al., 2017). Compared with pure LNF, LNFBY-1.00 displayed the characteristic bands of silicate and Si–O bending vibrations, while other bands related to LNF remained unchanged. The results indicated that the presence of muscovite did not alter the structure of LNF.

The full XPS spectra of the LNF and LNFBY-1.00 samples (Fig. 6b) indicated the presence of four elements (i.e. La, Ni, Fe, and O) in the two samples. In addition, Si and Al were also present in LNFBY-1.00. The binding energy obtained was corrected using the C 1s peak of 284.6 eV as a reference. According to the high-resolution spectrum of La 3d (Fig. 6c), La^{3+} $3d_{5/2}$ and La^{3+} $3d_{3/2}$ had binding energies of 833.8–833.9 eV and 850.4–850.8 eV (Schlapbach, 1981; Ye et al., 2020), respectively. Due to the strong overlap of the Ni $2p_{3/2}$ and La $3d_{3/2}$ peaks, the core-level spectrum of Ni $2p_{3/2}$ was difficult to determine. Therefore, the XPS spectra show the range of the Ni 2p peak and a part of

**Table 2** EDS data for BY, LNF, and LNFBY-1.00 samples (at.%)

Sample	O	Si	Al	K	La	Ni	Fe	Au
BY	62.34	13.37	11.48	3.97	/	/	2.71	6.13
LNF	55.92	/	4.15	/	18.94	16.39	0.98	3.62
LNFBY-1.00	63.53	12.35	10.79	3.28	2.16	1.74	2.25	3.90

the La $3d_{3/2}$ peak (Fig. 6d). Peaks at 852.8–853.9 eV and 854.8–855.8 eV were attributed to Ni^{2+} $2p_{3/2}$ and Ni^{3+} $2p_{3/2}$, respectively, while those at 871.4–872.5 eV and 878.9–879.4 eV belonged to Ni^{2+} $2p_{1/2}$ and Ni^{3+} $2p_{1/2}$ (Hüfner & Wertheim, 1975; Zhong et al., 2018), respectively. As indicated in the high-resolution spectrum of Fe 2p (Fig. 6e), the binding energies at 710.2–711.6 eV and 722.2–722.7 eV corresponded to Fe^{2+} $2p_{3/2}$ and Fe^{2+} $2p_{1/2}$, and 713.4–715.5 eV and 724.8–725.7 eV to Fe^{3+} $2p_{3/2}$ and Fe^{3+} $2p_{1/2}$ (Liu et al., 2019), respectively. In the high-resolution spectrum of O 1s (Fig. 6f), the peak binding energy 531.3–531.7 eV belonged to oxygen in the corresponding hydroxyl group and surface adsorbed oxygen, while 528.3–528.5 eV was assigned to lattice oxygen (Brundle, 1977; Dong et al., 2018; Zhu et al., 2020). In the LNFBY-1.00 composite sample, the binding energy of 529.9 eV was attributed to oxygen in Si–O–La, Si–O–Ni, and Si–O–Fe (Chen et al., 2020; Li et al., 2018), which demonstrated that LNF nanoparticles and muscovite substrate were connected by ionic bonds; the

bonding formed a strong interaction at the interface, promoted electron transfer between Si and La, Fe, and Ni via oxygen atoms, improved the ability of charge transfer (Chen et al., 2019a, b), and simultaneously bound the LNF particles to prevent detachment from the muscovite carrier. In addition, the number of hydroxyl groups and surface-adsorbed oxygen in the LNFBY-1.00 composite sample exceeded that of the LNF sample, which indicated that more highly active oxygen species could be produced by the composite, thereby increasing the amount of active substances in the photocatalytic reaction and, more significantly, improving the photocatalytic activity.

Photocatalytic Activity

As can be seen from the degradation rate of MO of the LNFBY-x samples under visible-light irradiation with time (Fig. 7a), in the absence of catalyst, the extent of degradation was only 3% after 2 h of irradiation, which demonstrated that MO was relatively stable. With pure
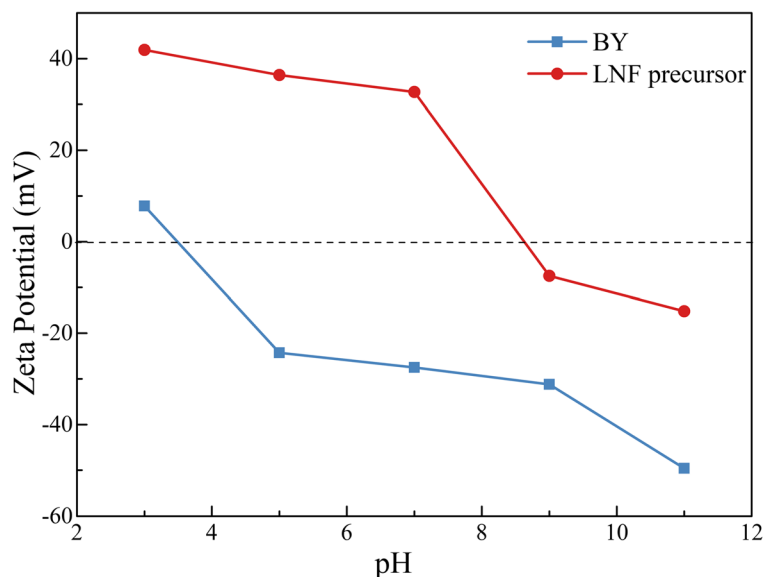
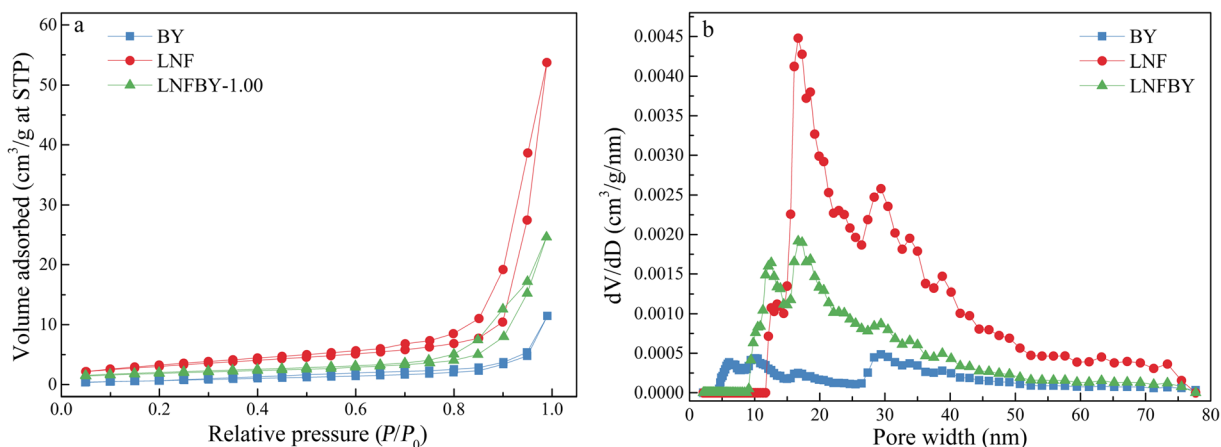**Fig. 4** pH and zeta potential diagram of the BY and LNF precursor

Fig. 5 **a** N$_2$ adsorption-desorption isotherms and **b** pore-width distribution curves of the BY, LNF, and LNFBY-1.00 samples

muscovite, the MO removal was only 33.1%, mainly due to physical adsorption. When the composite catalyst was added, the degradation of MO increased clearly. Using the extent of degradation of MO as an indicator to assess the photocatalytic activity, the photocatalytic activity decreased in the order LNFBY-1.00 > LNFBY-0.71 > LNF > LNFBY-5.00 > LNFBY-1.67 > LNFBY-0.56 > LNFBY-0.50 > BY. Therefore, one concludes that the enhancement in photocatalytic activity is related to the degree of dispersion of LNF nanoparticles and the characteristics of the muscovite carrier. At a mass ratio of LNF nanoparticles to muscovite of <1, some of the LNF nanoparticles did not compound completely with muscovite but formed agglomerated particles, some of which did not contribute effectively to the photocatalytic reactions. Such agglomeration resulted in the exposure of fewer photocatalytically active sites, thereby resulting in an insignificant improvement in the photocatalytic effect. When the mass ratio of LNF nanoparticles to muscovite reached a value of 1.00, however, LNF nanoparticles were dispersed evenly on the surface of muscovite, and the exposure of active sites was large. Furthermore, muscovite exhibited the unique adsorption characteristics of clay minerals, which could adsorb pollutants on the surface of the photocatalyst, achieving complete contact of the active sites with the pollutants and improving photocatalytic performance. Furthermore, the highly active oxygen-containing groups generated by the composite increased the amount of active substances in the photocatalytic reaction, which could be beneficial for improving photocatalytic activity. When the mass ratio of LNF nanoparticles to muscovite

was >1.00, excessive muscovite blocked light to a certain extent, thereby reducing the transmittance of the system, the number of photons, and the photocatalytic activity. The fitting results of pseudo-first order kinetics of the experimental data of the photocatalytic degradation by the LNFBY-x samples (Fig. 7b) showed good linearity. LNFBY-1.00 demonstrated the greatest degradation-rate constant (0.0278 min^{-1}), which was 1.03 times greater than that of LNF (0.0270 min^{-1}). In recent years, the loading of photocatalytic materials on the surface of other carriers such as montmorillonite and kaolinite has, increasingly, been investigated (Fufa et al., 2022; Lin et al., 2017; Yan et al., 2019). Although the specific surface area and dispersion of the photocatalytic materials have increased, their photocatalytic activity was still less than that of LNFBY-1.00. A possible reason was that these photocatalytic materials cannot form chemical bonds to the surfaces of these carriers, and cannot provide further catalytic reaction sites to enhance photocatalytic activity. In practice, its shedding and separation is also a key problem. Thus, muscovite with a natural flaky morphology could be an excellent carrier material for photocatalytic perovskite-type oxide materials, capable of controlling effectively the size of LNF nanoparticles, hindering agglomeration, improving dispersibility, exposing more catalytic reaction sites, and improving the utilization rate of photocatalytic materials, especially that of the highly active oxygen species produced by the composite, which could increase the number of active substances in the photocatalytic process. Thus, it could be conducive to photocatalytic reaction.
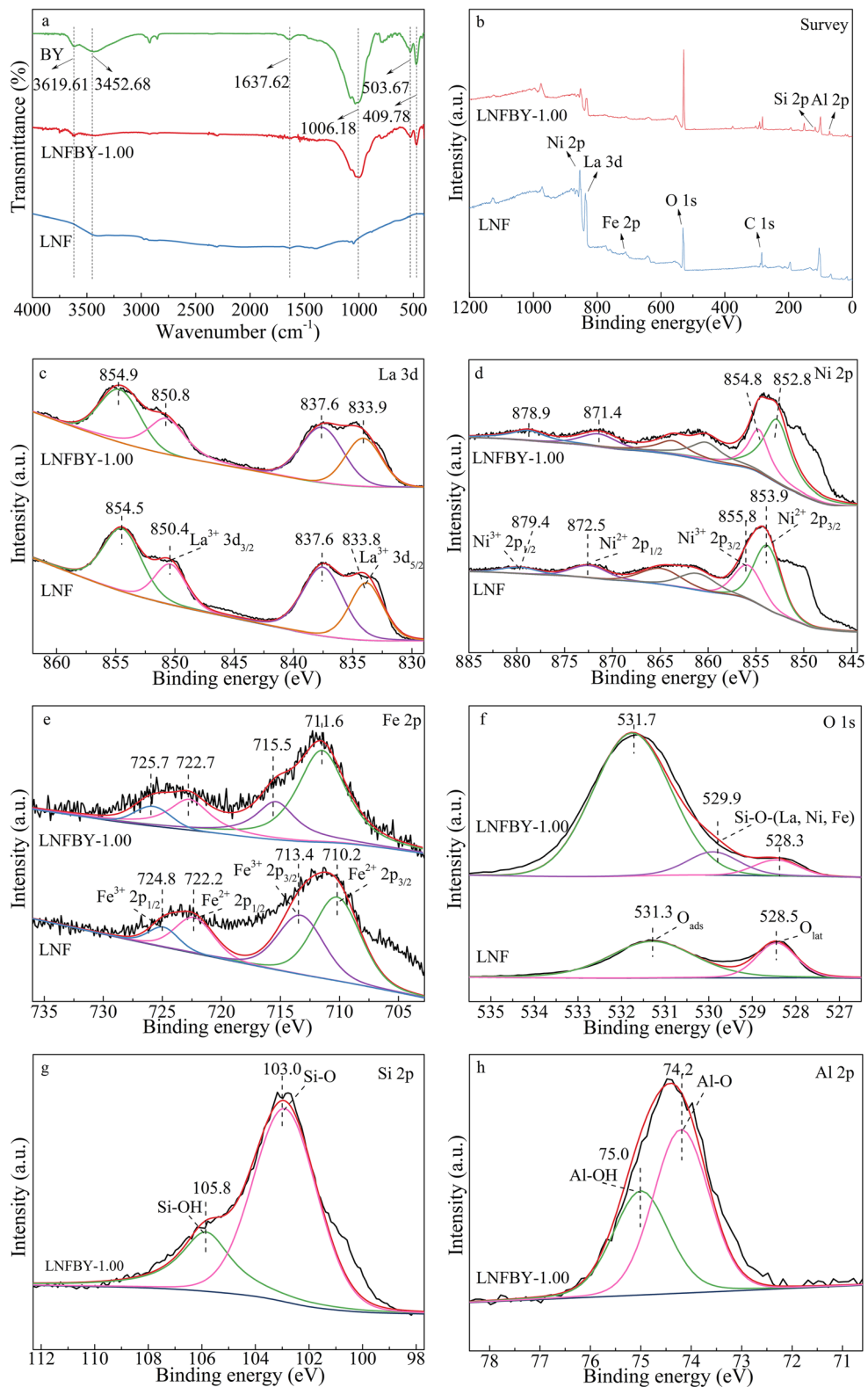
Springer

Fig. 6 **a** FTIR spectra of the BY, LNF, and LNFBY-1.00 samples; **b–f** XPS spectra of LNF and LNFBY-1.00 samples; **b** Survey, **c** La 3d, **d** Ni 2p, **e** Fe 2p, **f** O 1s; **g–h** XPS spectra of LNFBY-1.00; **g** Si 2p, **h** Al 2p
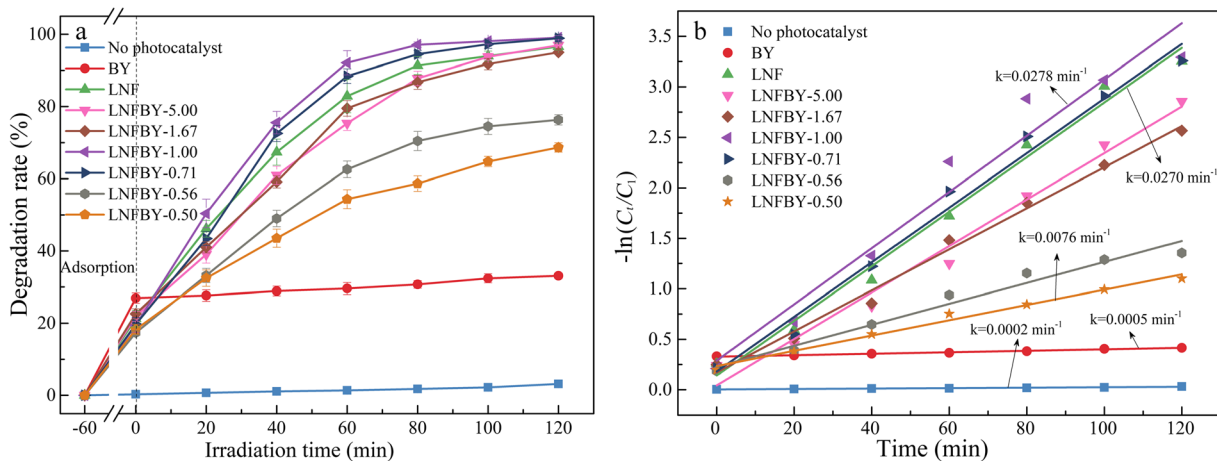
🖄 Springer

Fig. 7 **a** Degradation rate of MO by LNFBY-*x* series samples; **b** photocatalytic degradation reactions of LNFBY-*x* series samples were fitted using quasi-first order kinetics

Stability and Recyclability

The degradation rate of MO of the LNFBY-1.00 sample under visible-light irradiation for 2 h after five consecutive cycles (Fig. 8) showed that the degradation rate of MO tended to decrease. After five cycles, the MO degradation rate by LNFBY-1.00 was 75.75%, which still showed high catalytic activity. Compared with pure LNF, the LNFBY-1.00 sample could be recovered more easily via filtration and natural sedimentation, which would significantly reduce the cost of catalyst recovery. As an explanation for the slight decrease in

photocatalytic performance, residual MO, adsorbed on the catalyst during the photocatalytic degradation process, might be present, and some active sites remained occupied.

Photocatalytic Mechanism

The MO degradation rates of LNFBY-1.00 with time after addition of various trapping agents (Fig. 9a) showed that the degradation rate of MO decreased after the addition of each scavenger. Compared to the other agents, the addition of IPA exerted less effect on the

Fig. 8 Recyclability of MO degradation in a LNFBY-1.00 sample after 2 h of visible light irradiation
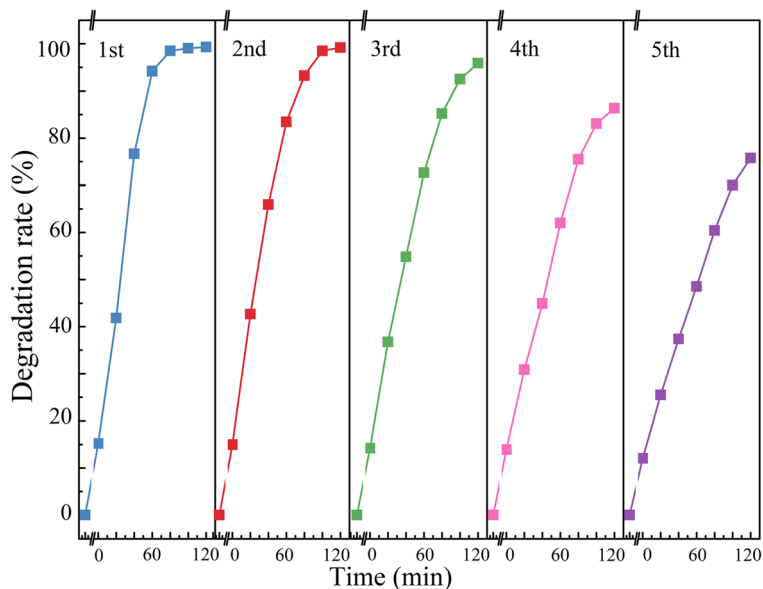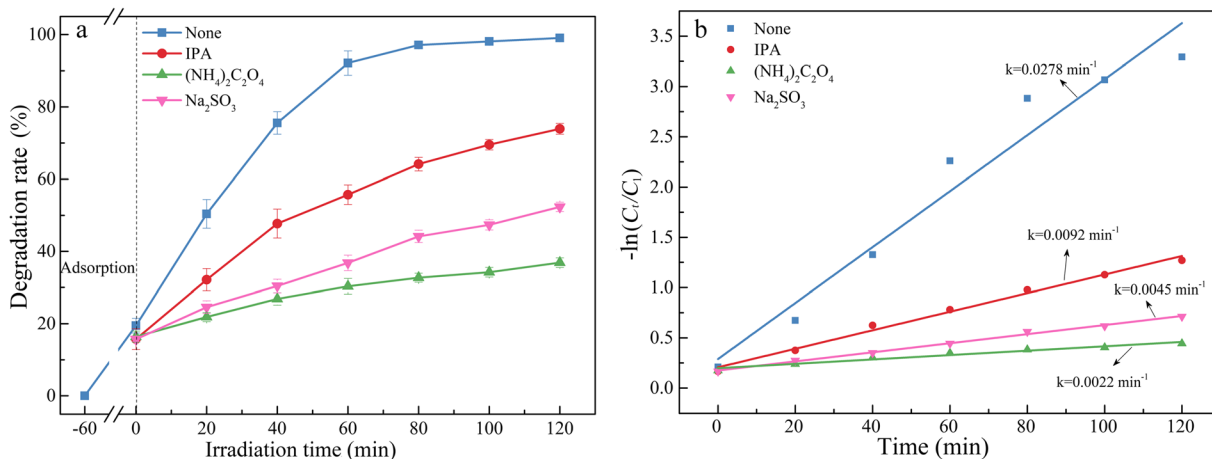
Fig. 9 **a** Effect of three different free radical capture agents on the degradation rates of MO; **b** photocatalytic degradation reactions were fitted with quasi-first order kinetics

degradation rate of MO, probably because the production of $\cdot OH$ was lower. With the addition of Na_2SO_3 to the system, the degradation rate decreased, which demonstrated that e^- contributed to a certain degree to MO degradation. In the presence of $(NH_4)_2C_2O_4$, the degradation rate dropped significantly, thereby demonstrating h^+ as the major active substance in the photocatalytic degradation of MO. The contribution of the active free radicals decreased in the order $h^+ > e^- > \cdot OH$.

Based on the test results for the active species, the following degradation mechanism may be present (Fig. 10): LNF nanoparticles are excited by visible light with energy exceeding the threshold value to generate e^--h^+ pairs, and the negatively charged e^- reacts with O_2 adsorbed on the catalyst surface to generate superoxide radicals ($\cdot O_2^-$), thereby leading to MO degradation. Some h^+ oxidized OH^- and H_2O in solution to produce

hydroxyl radicals ($\cdot OH$), exhibiting high activity and participating in the degradation reaction. Some h^+ interacted directly with MO. In such a process, the interfacial interaction between LNF nanoparticles and the muscovite substrate improved the charge transferability of the composite sample, thereby improving the photocatalytic reaction. In addition, the great adsorption performance by the muscovite support could result in a higher apparent MO concentration on the surface of the catalytic material, thereby further elevating the photocatalytic degradation rate.

Conclusions

(1) A series of LNFBY-x samples was synthesized by a sol-gel impregnation method from LNF nanoparticles

Fig. 10 Degradation mechanism diagram of the LNFBY-1.00 sample
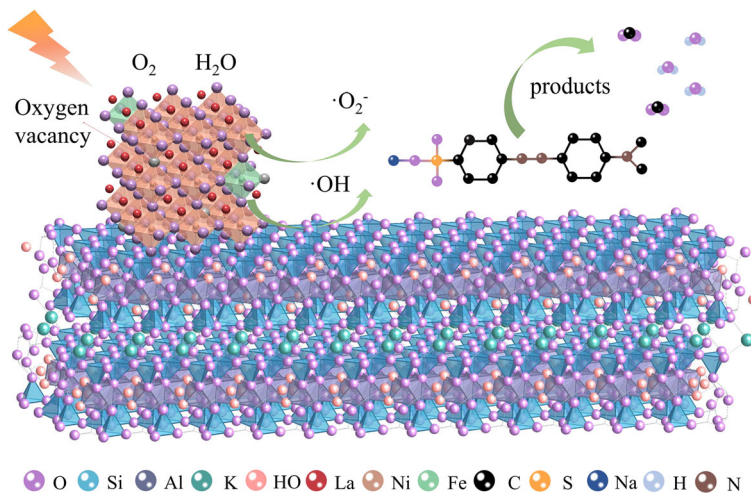
and muscovite. The two components were connected firmly by ionic bonds without altering the phase and structure. Compounding with muscovite effectively controls the size of LNF nanoparticles and prevents agglomeration, thereby exposing more catalytic reaction sites and improving the utilization rate of the photocatalytic materials. The highly reactive oxygen species produced by the composite increased the amount of active substances in the photocatalytic process and enhanced the photocatalytic activity.

(2) Among the LNFBY-x samples, the LNFBY-1.00 (mass ratio of LNF to muscovite = 1.00) demonstrated the best structure and photocatalytic performance. The degradation rate of MO reached 99.03% after visible-light irradiation for 120 min. After five catalyst recycles, the MO degradation rate of the LNFBY-1.00 sample was 75.75%, which is still considered high catalytic activity. In the degradation process, the contribution of active free radicals decreased in the order h^+ > e^- > $\cdot OH$.

(3) The reason for the enhanced photocatalytic activity was the binding of LNF nanoparticles to the muscovite substrate, thereby hindering the agglomeration of LNF nanoparticles. Therefore, the composite samples exhibited smaller particle sizes, larger specific surface areas, moderate pore size distributions, and strong adsorption capacity. In addition, the interfacial interaction between LNF nanoparticles and the muscovite substrate enhances the charge transferability of the composite sample, thereby improving the photocatalytic reaction. Furthermore, the concentration of MO around LNF nanoparticles was enhanced through adsorption by muscovite, thereby increasing the contact probability of LNF and MO molecules and ultimately improving the photocatalytic degradation rate.

Declarations

Consent for publication The authors declared their consent for publication.

Conflict of interest The authors declare that they have no conflict of interest.

References

Asencios, Y. J. O., Quijo, M. V., Marcos, F. C. F., Nogueira, A. E., Rocca, R. R., & Assaf, E. M. (2019). Photocatalytic activity of Nb heterostructure ($NaNbO_3/Na_2Nb_4O_{11}$) and Nb/clay materials in the degradation of organic compounds. *Solar Energy, 194*, 37–46.

Bao, T., Damtie, M. M., Hosseinzadeh, A., Frost, R. L., Yu, Z. M., Jin, J., & Wu, K. (2020). Catalytic degradation of P-chlorophenol by muscovite-supported nano zero valent iron composite: Synthesis, characterization, and mechanism studies. *Applied Clay Science, 195*, 105735–105746.

Barakat, M. A., Kumar, R., Lima, E. C., & Seliem, M. K. (2021). Facile synthesis of muscovite–supported Fe_3O_4 nanoparticles as an adsorbent and heterogeneous catalyst for effective removal of methyl orange: Characterisation, modelling, and mechanism. *Journal of the Taiwan Institute of Chemical Engineers, 119*, 146–157.

Belver, C., Bedia, J., Álvarez-Montero, M.A., & Rodriguez, J.J. (2016). Solar photocatalytic purification of water with Ce-doped TiO_2/clay heterostructures. *Catalysis Today, 266*, 36-45.

Brundle, C. R. (1977). Oxygen adsorption and thin oxide formation at iron surfaces: An XPS/UPS study. *Surface Science, 66*, 581–595.

Chen, Y., Wu, Q., Bu, N., Wang, J., & Song, Y. (2019a). Magnetic recyclable lanthanum-nitrogen co-doped titania/strontium ferrite/diatomite heterojunction composite for enhanced visible-light-driven photocatalytic activity and recyclability. *Chemical Engineering Journal, 373*, 192–202.

Chen, Y., Wu, Q., Liu, L., Wang, J., & Song, Y. (2019b). The fabrication of floating Fe/N co-doped titania/diatomite granule catalyst with enhanced photocatalytic efficiency under visible light irradiation. *Advanced Powder Technology, 30*, 126–135.

Chen, Y., Wu, Q., Wang, J., & Song, Y. (2020). Visible-Light-Driven Mitigation of Rhodamine B and Disinfection of E. coli Using Magnetic Recyclable Copper–Nitrogen Co-doped Titania/Strontium Ferrite/Diatomite Heterojunction Composite. *Journal of Inorganic and Organometallic Polymers and Materials, 30*, 1065–1077.

Dong, X., Sun, Z., Zhang, X., Li, X., & Zheng, S. (2018). Synthesis and Enhanced Solar Light Photocatalytic Activity of a C/N Co-Doped TiO_2/Diatomite Composite with Exposed (001) Facets. *Australian Journal of Chemistry, 71*, 315–324.

Edward, S. (1982). Water in silicate glasses: an infrared spectroscopic study. *Contributions to Mineralogy & Petrology, 81*, 1–17.

Farmer, V. C. (1968). Infrared Spectroscopy in Clay Mineral Studies. *Clay Minerals, 7*, 373–387.

Fufa, P. A., Feyisa, G. B., Gultom, N. S., Kuo, D. H., Chen, X. Y., Kabtamu, D. M., & Zelekew, O. A. (2022). Visible light-driven photocatalytic activity of Cu_2O/ZnO/Kaolinite-based composite catalyst for the degradation of organic pollutant. *Nanotechnology, 33*, 315601–315612.

Fukina, D. G., Koryagin, A. V., Koroleva, A. V., Zhizhin, E. V., Suleimanov, E. V., & Kirillova, N. I. (2021). Photocatalytic properties of β-pyrochlore RbTe1.5W0.5O6 under visible-

light irradiation. *Journal of Solid State Chemistry, 300*, 122235.

Gong, C., Xiang, S., Zhang, Z., Sun, L., Ye, C., & Lin, C. (2019). Construction and Visible-Light-Driven Photocatalytic Properties of $LaCoO_3$-TiO_2 Nanotube Arrays. *Acta Physico-Chimica Sinica, 35*, 616–623.

Hüfner, S., & Wertheim, G. K. (1975). Systematics of core line asymmetries in XPS spectra of Ni. *Physics Letters A, 51*, 301–303.

Ismael, M., & Wu, Y. (2019). A facile synthesis method for fabrication of $LaFeO_3$/g-C_3N_4 nanocomposite as efficient visible-light-driven photocatalyst for photodegradation of RhB and 4-CP. *New Journal of Chemistry, 43*, 13783–13793.

Khaledian, H. R., Zolfaghari, P., Nezhad, P. D. K., Niaei, A., Khorram, S., & Salari, D. (2021). Surface modification of $LaMnO_3$ perovskite supported on CeO_2 using argon plasma for high-performance reduction of NO. *Journal of Environmental Chemical Engineering, 9*, 104581–104589.

Khan, I., Khan, I., Usman, M., Imran, M., & Saeed, K. (2020). Nanoclay-mediated photocatalytic activity enhancement of copper oxide nanoparticles for enhanced methyl orange photodegradation. *Journal of Materials Science: Materials in Electronics, 31*, 8971–8985.

Khatri, A., & Rana, P. S. (2020). Visible light assisted photocatalysis of Methylene Blue and Rose Bengal dyes by iron doped NiO nanoparticles prepared via chemical co-precipitation. *Physica B: Condensed Matter, 579*, 411905–411913.

Kim, W. Y., Jang, J. S., Ra, E. C., Kim, K. Y., Kim, E. H., & Lee, J. S. (2019). Reduced perovskite $LaNiO_3$ catalysts modified with Co and Mn for low coke formation in dry reforming of methane. *Applied Catalysis A: General, 575*, 198–203.

Landge, V. K., Sonawane, S. H., Sivakumar, M., Sonawane, S. S., Uday Bhaskar Babu, G., & Boczkaj, G. (2021). S-scheme heterojunction Bi_2O_3-ZnO/Bentonite clay composite with enhanced photocatalytic performance. *Sustainable Energy Technologies and Assessments, 45*, 101194–101203.

Li, X., Tang, C., Zheng, Q., Shao, Y., & Li, D. (2017a). Amorphous MoSx on CdS nanorods for highly efficient photocatalytic hydrogen evolution. *Journal of Solid State Chemistry, 246*, 230–236.

Li, X., Yan, X., Zuo, S., Lu, X., Luo, S., Li, Z., Yao, C., & Ni, C. (2017b). Construction of $LaFe_{1-x}Mn_xO_3$/attapulgite nanocomposite for photo-SCR of NO_x at low temperature. *Chemical Engineering Journal, 320*, 211–221.

Li, X., Peng, K., Chen, H., & Wang, Z. (2018). TiO_2 nanoparticles assembled on kaolinites with different morphologies for efficient photocatalytic performance. *Scientific Reports, 8*, 11663.

Li, Y., Sun, H., Peng, T., You, H., Qin, Y., & Zeng, L. (2019). Effects of muscovite matrix on photocatalytic degradation in TiO_2/muscovite nanocomposites. *Applied Clay Science, 179*, 105155–105164.

Lin, L., Song, Y., Bo, J., Wang, K., & Qian, Z. (2017). A novel oxygen carrier for chemical looping reforming: $LaNiO_3$ perovskite supported on montmorillonite. *Energy, 131*, 58–66.

Liu, H., Yi, Y., Qin, Z., Wu, Y., Li, L., Chu, B., Jin, G., Li, R., Tong, Z., Dong, L., & Li, B. (2019). In Situ Diffuse Reflectance Infrared Fourier Transform Spectroscopy Study of NO + CO Reaction on $La0.8Ce_{0.2}Mn_{1-x}Fe_xO_3$

Perovskites: Changes in Catalytic Properties Caused by Fe Incorporation. *Industrial & Engineering Chemistry Research, 58*, 9065–9074.

Maeda, K., Eguchi, M., & Oshima, T. (2014). Perovskite Oxide Nanosheets with Tunable Band-Edge Potentials and High Photocatalytic Hydrogen-Evolution Activity. *Angewandte Chemie International Edition, 53*, 13164–13168.

Maridevaru, M. C., Wu, J. J., Viswanathan Mangalaraja, R., & Anandan, S. (2020). Ultrasonic-Assisted Preparation Of Perovskite-Type Lanthanum Nickelate Nanostructures and Its Photocatalytic Properties. *ChemistrySelect, 5*, 7947–7958.

Peng, F., Ni, Y., Zhou, Q., Kou, J., Lu, C., & Xu, Z. (2018). New g-C_3N_4 based photocatalytic cement with enhanced visible-light photocatalytic activity by constructing muscovite sheet/SnO_2 structures. *Construction and Building Materials, 179*, 315–325.

Peng, K., Fu, L., Yang, H., & Ouyang, J. (2016). Perovskite $LaFeO_3$/montmorillonite nanocomposites: synthesis, interface characteristics and enhanced photocatalytic activity. *Scientific Reports, 6*, 19723–19733.

Purohit, S., Yadav, K. L., & Satapathi, S. (2021). Bandgap Engineering in a Staggered-Type Oxide Perovskite Heterojunction for Efficient Visible Light-Driven Photocatalytic Dye Degradation. *Langmuir, 37*, 3467–3476.

Salam, M. A., Abukhadra, M. R., & Mostafa, M. (2020). Effective decontamination of As(V), Hg(II), and U(VI) toxic ions from water using novel muscovite/zeolite aluminosilicate composite: adsorption behavior and mechanism. *Environmental Science and Pollution Research, 27*, 13247–13260.

Schlapbach, L. (1981). XPS/UPS study of the oxidation of La and $LaNi_5$ and of the electronic structure of $LaNi_5$. *Solid State Communications, 38*, 117–123.

Shao, P., Siao, Y., Lai, Y., Hsieh, P., Tsao, C., Lu, Y., Chen, Y., Hsu, Y., & Chu, Y. (2021). Flexible $BiVO_4$/WO_3/ITO/Muscovite Heterostructure for Visible-Light Photoelectrochemical Photoelectrode. *ACS Applied Materials & Interfaces, 13*, 21186–21193.

Shi, H., Li, X., Xia, J., Lu, X., Zuo, S., Luo, S., & Yao, C. (2017). Sol-gel Synthesis of $LaBO_3$/Attapulgite (B=Mn, Fe, Co, Ni) Nanocomposite for NH3-SCR of NO at Low Temperature. *Journal of Inorganic and Organometallic Polymers and Materials, 27*, 166–172.

Tahir, M., Tahir, B., Zakaria, Z. Y., & Muhammad, A. (2019). Enhanced photocatalytic carbon dioxide reforming of methane to fuels over nickel and montmorillonite supported TiO_2 nanocomposite under UV-light using monolith photoreactor. *Journal of Cleaner Production, 213*, 451–461.

Touaa, N. D., Bouberka, Z., Gherdaoui, C. E., Supiot, P., Roussel, P., Pierlot, C., & Maschke, U. (2020). Titanium and iron-modified delaminated muscovite as photocatalyst for enhanced degradation of Tetrabromobisphenol A by visible light. *Functional Materials Letters, 13*, 2051008.

Tun, P., Wang, K., Naing, H., Wang, J., & Zhang, G. (2019). Facile preparation of visible-light-responsive kaolin-supported Ag@AgBr composites and their enhanced photocatalytic properties. *Applied Clay Science, 175*, 76–85.

Wang, X., Mu, B., Hui, A., & Wang, A. (2019). Comparative study on photocatalytic degradation of Congo red using different clay mineral/CdS nanocomposites. *Journal of Materials Science: Materials in Electronics, 30*, 5383–5392.

Xu, B., Maimaiti, H., Wang, S., Awati, A., Wang, Y., Zhang, J., & Chen, T. (2019). Preparation of coal-based graphene oxide/ SiO_2 nanosheet and loading ZnO nanorod for photocatalytic Fenton-like reaction. *Applied Surface Science, 498*, 143835–143846.

Yan, C., Qiong, W., Li, L., Jun, W., & Ytao, S. (2019). The fabrication of self-floating Ti^{3+}/N co-doped TiO_2/diatomite granule catalyst with enhanced photocatalytic performance under visible light irradiation. *Applied Surface Science, 467-468*, 514–525.

Yang, X., Ke, X., Yang, D., Liu, J., Guo, C., Frost, R., Su, H., & Zhu, H. (2010). Effect of ethanol washing of titania clay mineral composites on photocatalysis for phenol decomposition. *Applied Clay Science, 49*, 44–50.

Ye, Y., Yang, H., Zhang, H., & Jiang, J. (2020). A promising Ag_2CrO_4/$LaFeO_3$ heterojunction photocatalyst applied to photo-Fenton degradation of RhB. *Environmental Technology, 41*, 1486–1503.

Zhong, W., Jiang, T., Dang, Y., He, J., Chen, S., Kuo, C., Kriz, D., Meng, Y., Meguerdichian, A. G., & Suib, S. L. (2018). Mechanism studies on methyl orange dye degradation by perovskite-type $LaNiO_{3-\delta}$ under dark ambient conditions. *Applied Catalysis A: General, 549*, 302–309.

Zhou, S., Lv, J., Guo, L. K., Xu, G. Q., Wang, D. M., Zheng, Z. X., & Wu, Y. C. (2012). Preparation and photocatalytic properties of N-doped nano-TiO_2/muscovite composites. *Applied Surface Science, 258*, 6136–6141.

Zhu, W., Chen, X., Liu, Z., & Liang, C. (2020). Insight into the Effect of Cobalt Substitution on the Catalytic Performance of $LaMnO_3$ Perovskites for Total Oxidation of Propane. *The Journal of Physical Chemistry C, 124*, 14646–14657.

⚛ Springer